Astron. Astrophys. 329, 249–264 (1998)

ASTRONOMY
AND
ASTROPHYSICS

Clump mass spectra of molecular clouds

C. Kramer[1⋆], **J. Stutzki**[2], **R. Röhrig**[2], **and U. Corneliussen**[2]

[1] Instituto de Radioastronomía Milimétrica (IRAM), Avenida Divina Pastora 7, Núcleo Central, E-18012 Granada, Spain
[2] I. Physikalisches Institut, Universität zu Köln, Zülpicher Straße 77, D-50937 Köln, Germany

Received 30 October 1996 / Accepted 21 July 1997

Abstract. We present clump mass spectra of the seven molecular clouds L1457, MCLD 126.6 + 24.5, NGC 1499 SW, Orion B South, S140, M17 SW, and NGC 7538, which were derived by a Gaussian clump decomposition algorithm from large scale isotopomeric CO maps.

We discuss in detail the reliability of the mass spectra derived by studying their dependence on the control parameters of the decomposition algorithm.

All clump mass spectra found are consistent with a power law, $dN/dM \propto M^{-\alpha}$, with α between 1.6 and 1.8. Due to the different resolution of the observations and the different distances of the clouds, the clump masses range from several 10^4 $M_\odot$ in NGC 7538 down to 10^{-4} $M_\odot$, less than the mass of Jupiter, in the nearby cloud L1457. The large dynamic range covered by the observations is reflected by the high number of clumps found in each cloud, which lie between 100 and 1300. The spectral index of the clump mass distributions thus is independent of the wide range of physical properties of the clouds studied. In particular, there are no indications of a turnover of the clump mass power law index at a characteristic clump mass such as the Jeans mass, below which the clumps become gravitationally unbound. This is particularly emphasized by the clump properties in L1457 most of which are clearly substellar and which are far from being gravitationally bound objects.

Key words: interstellar medium: clouds – structure – molecules

1. Introduction

Molecular clouds show structure on all scales observed. The observed intensity distribution often allows to identify subunits well separated from each other. The structure thus is often called clumpy. Individual clumps become most clearly visible at high spectral resolution, either in a series of channel maps or in velocity-position diagrams. Whether the observed intensity distribution can be separated into individual clumps crucially depends on the velocity resolution and source intrinsic velocity dispersion. If the clump to clump dispersion is not significantly larger than the clump intrinsic line width, or if the velocity resolution given by the observational parameters is too low, the individual clumps are blended into a smoother distribution. In addition, experience has shown that the structure breaks up further if observed at yet higher spatial resolution (see e.g. Langer et al. 1995). Thus, the structure observed changes with the spatial resolution of the observations. There is good indication that the structure is likely to be self similar over a large range of length scales. This is indicated by its characterization in terms of fractal parameters, e.g. the power law shape of the area-perimeter relation of iso-intensity contours (Falgarone et al. 1991, Zimmermann & Stutzki 1993) or by the power law shape of the image power spectra for HI clouds (Green 1993) and for molecular clouds (Scalo 1985, Stutzki et al. 1997).

Several different methods have been developed over the past years to characterize the clumpy structure. With an individual clump identified, its size, line width, and other parameters can be determined. One of the more fundamental parameters of a clump is its mass. The mass is generally derived via the integrated intensity of an optically thin line, which gives the column density along the line of sight, and then the mass by integrating over the clump area. The clump mass is thus a very robust parameter and does not depend on the actual spatial or velocity resolution (unless small size clumps blend into a larger clump). In all cases where clump masses have been derived for a significantly large number of clumps, the different methods agree in showing a clump mass spectral distribution following a power law mass spectrum of the form $dN/dM \propto M^{-\alpha}$ with the power law spectral index α in the range 1.4 to 1.9 (see a review by Blitz 1993). Although the presence of a power law mass spectrum over at least an order of magnitude in mass is firmly established only in a few cases where the source structure (velocity dispersion) and the quality of the observational data (area coverage, signal to noise ratio) allow a systematic analysis, it seems to be a general property of molecular cloud structure. As a power law mass spectrum with $\alpha > 0$ predicts an increasing number of smaller and smaller clumps, confusion is usually the limiting

Send offprint requests to: C. Kramer, (kramer@ph1.uni-koeln.de)
⋆ *Present address:* I. Physikalisches Institut, Universität zu Köln, Zülpicher Straße 77, 50937 Köln, Germany

factor in clump identification by eye. Nevertheless, a number of papers report clump mass spectra derived over a limited range of masses by eye inspection (Carr 1987; Loren 1989; Nozawa et al. 1991; Lada et al. 1991a; cf Blitz 1993; Dobashi et al. 1996). It is thus highly desirable to use automated clump finding algorithms in the analysis of observed data. In addition, the use of an algorithm allows to analyze the structure in a consistent, stable way – within the dataset of one cloud and for several clouds. One such method has been presented by Stutzki & Güsten (1990), hereafter SG90, who developed a modified least square fitting procedure, hereafter called GAUSSCLUMPS, to decompose the observed 3-dimensional data cubes (2 spatial coordinates, one spectral coordinate) into a series of clumps, which are assumed to have Gaussian shape.

Some aspects of the reliability of the Gaussian clump decomposition algorithm were already tested by SG90 by simulations with artificially generated clump ensembles. The power law index of artificially created clump ensembles was reproduced by the algorithm to within less than 0.1 in the range α = 1.1 to 1.75.

Stutzki & Güsten used the method for an analysis of a $C^{18}O(2\rightarrow1)$ map of the M17 SW cloud core and decomposed it into about 170 clumps. The method has been applied by a number of other authors (Hobson 1992; Johnen 1992; Herbertz 1992; Zimmermann 1993; Hobson et al. 1994; Kramer et al. 1996; Röhrig 1996; Corneliussen 1996; Wiesemeyer et al. 1996), and the resulting clumps have been compared with independent images observed in high density tracers (Wang et al. 1993).

Another method has been developed by Williams et al. (1994, 1995), who decompose an observed image into a number of clumps by assigning each volume element of the 3-dimensional data cube to one of the local maxima identified in the observed intensity distribution. In their method the number of clumps is thus limited exactly to the number of local maxima in the observed data cube, and the shape of the clumps identified is arbitrary. They used this algorithm to analyze data on the Rosette Molecular Cloud and the Maddalena cloud. Although the basic concept of both algorithms is quite different, they give consistent results for the larger clumps, when used on the same data (Williams et al. 1994). In the lower mass range, the emission is assigned to additional smaller clumps in the Gaussian decomposition algorithm, and is assigned to the irregular extensions of the more massive clumps in the Willams et al. approach.

Still another method was developed by Langer et al. (1993), who analyzed the structure of the cold, dark cloud B5 by applying Laplacian pyramid transforms, a form of nonorthogonal wavelets, on CO maps of *integrated* intensities. Again, this procedure allows to identify clumps and to derive the number distribution of clump masses, although the structural information, present in the spectral dimension, is not exploited.

Elmegreen & Falgarone (1997) use the fractal dimension of the observed intensity distributions of five cloud surveys taken from the literature, together with a mass-size relation of the clumps identified, to derive mass spectral indices between 1.6 and 2.0.

The physical reality of the clumps identified has been a matter of controversial debate since presentation of the first systematic attempts to identify clumps. The original hope, of course, was that the clumps identified would represent the cloud substructures finally forming individual stars. This view is supported by a possible connection between the power law index of the clump mass spectrum and the power law index of the initial mass function (Zinnecker 1989). It is also supported by the observed fact, that the local efficiency of star formation can be very high: young stellar clusters, which recently became accessible to observations by the rapid progress in IR array technology, show a very large number of stars over a wide range of masses and a density of stars that, if smeared out, implies densities in the high range of molecular cloud core densities. Examples are the Trapezium cluster (McCaughrean & Stauffer 1994) in Orion A, the NGC 2024 cluster in Orion B (Lada et al. 1991b), and the IC348 cluster (Lada & Lada 1995) in the Perseus cloud. Rapid conversion of the whole cloud core within a short time scale thus seems to be necessary, implying that the resulting stellar initial mass function might be related to the clumpy structure of the core immediately before the collapse.

The Gaussian clump decomposition procedure meanwhile has been used on a large number of data sets on a wide variety of molecular clouds. These data were obtained at different telescopes and thus reach different angular and linear resolutions. In all cases but one, ^{13}CO and $C^{18}O$ were used as tracers of molecular column densities. As the smallest mass identifiable above the noise limit is given by the product of the noise level, the velocity resolution (or clump intrinsic line width) and the linear resolution (i.e. the angular resolution and the source distance), these data cover a wide range of masses. The purpose of this paper is to present the results of the Gaussian decomposition on this large set of observations. Along the way, we also discuss the important aspect of the possible systematic errors and the confusion introduced near the noise limit, and how these influence the mass spectra derived.

2. Observations

We analyze large scale mapping surveys of the molecular clouds L1457, MCLD 126.6 + 24.5, NGC 1499 SW, Orion B South, S140, M17 SW, and NGC 7538, partly named after their associated H II regions. These clouds were observed in the years 1990 to 1995 with the KOSMA 3m radio telescope, the Nagoya 4m telescope, the FCRAO 15m telescope, or the IRAM 30m telescope. The GAUSSCLUMPS algorithm was applied to the three dimensional emission line data of one of the two lowest rotational transitions of $C^{18}O$, ^{13}CO, or, in one case, ^{12}CO (Table 1).

The clouds observed differ widely in their physical properties: they span the range from small, dark, cold, and inactive molecular cloudlets to giant molecular clouds exhibiting ongoing formation of massive stars.

The high-latitude dark cloud L1457, at a distance to the sun of only 65 pc, lies at the edge of the local bubble of hot ionized gas (see Moriarty-Schieven et al. 1997) and to the west

Table 1. Observations. Column (1) gives the halfpower beam width and column (2) the spatial sampling chosen for the mappings. Column (3) gives the velocity resolution of the spectrometer backend used. The average rms temperature $T_{\rm mb}^{\rm rms}$ achieved at the given spectral resolution are quoted in column (4). The next two columns are included to quantify the quality of the datasets, i.e. the dynamic ranges reached. Column (5) gives the spectral dynamic range, that is the ratio of maximum linewidth over velocity resolution. Column (6) gives the peak signal to noise ratio. The number of positions observed with the given spatial sampling is listed in column (7).

		HPBW ["] (1)	grid ["] (2)	$\Delta v_{\rm res}$ [ms^{-1}] (3)	$T_{\rm mb}^{\rm rms}$ [K] (4)	$\frac{\Delta v_{\rm max}}{\Delta v_{\rm res}}$ (5)	S/N (6)	Pos. (7)
L1457-S	^{13}CO(2→1)	12	7.5	190	0.2	13	37	4000
S140	C^{18}O(2→1)	13	7.5	190	0.6	13	20	1100
MCLD 126.6 + 24.5	^{12}CO(2→1)	125	120	60	0.2	20	15	211
M17 SW	C^{18}O(2→1)	13	15,7.5	190	0.6	16	40	280
Orion B-S	^{13}CO(2→1)	125	120	370	0.26	11	70	660
NGC 1499 SW	^{13}CO(1→0)	180	240	200	0.2	12	20	750
NGC 7538	C^{18}O(1→0)	50	25	1200	0.07	6	16	2520
NGC 7538	^{13}CO(1→0)	50	25	1200	0.25	6	36	3720

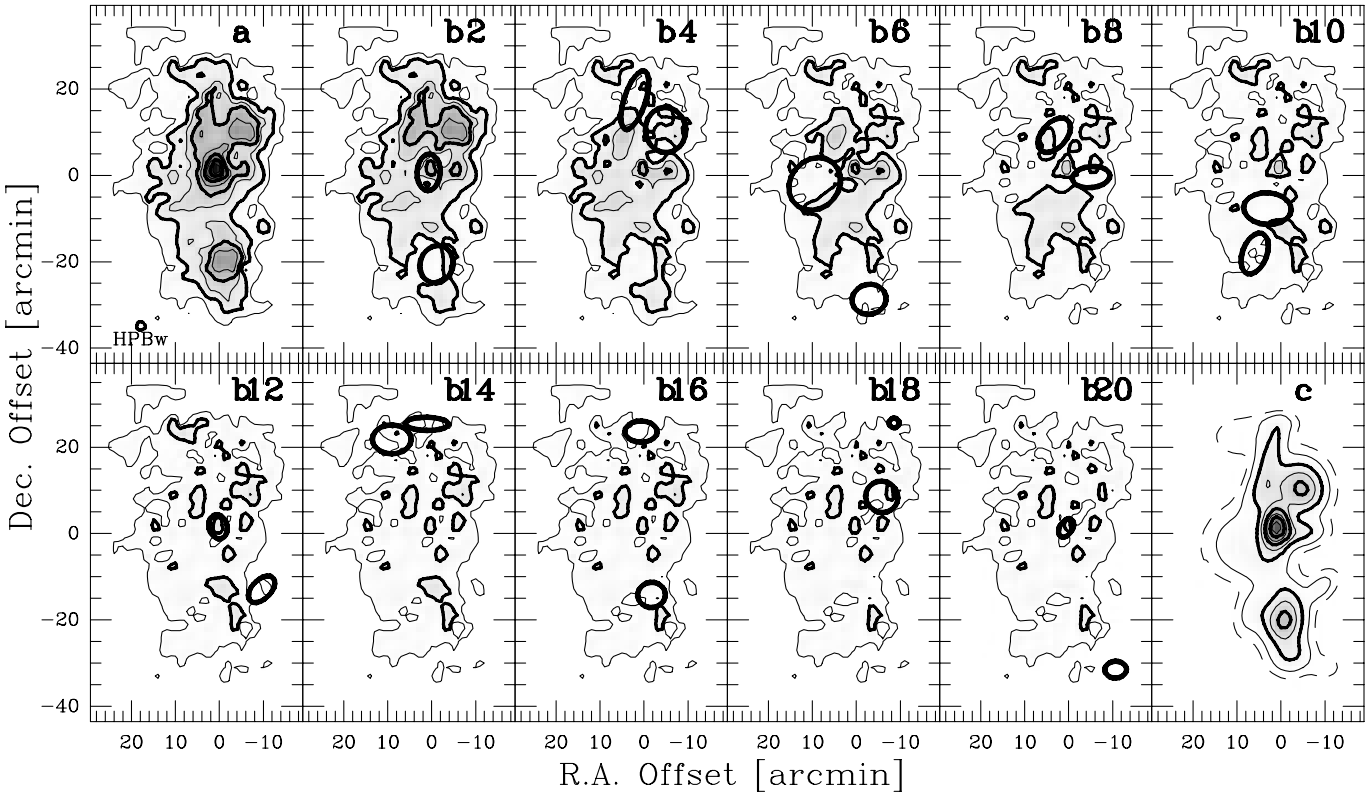

Fig. 1. Orion B South. **a** The original map of integrated ^{13}CO(2→1) intensities. **b2** to **b20** The maps after subtraction of 2 to 20 clumps by GAUSSCLUMPS (stiffness parameters: s_0 = 5, s_a = s_c = 1). The spatial (not deconvolved) FWHMs of the last two clumps subtracted are shown. **c** Integrated intensity of the first 20 clumps identified by the algorithm. The range of integration is 0 to 20 kms^{-1} and contours are at 5.7 (=8σ), 12 by 6 to 60 Kkms^{-1}. The dashed contour in **c** is 5% of the maximum. The tiny clump in panel b18 is due to a single channel spike in the corresponding spectrum and is ignored by the follow up analysis of clumps fitted.

of the Taurus complex of dark clouds (Ungerechts & Thaddeus 1987). The cloud exhibits only moderate, if any, star formation activity. Only five young stellar objects have been tentatively detected so far. Pound & Blitz (1993) find indications for a self-gravitating core. ^{13}CO observations at arcminute resolutions (Zimmermann & Ungerechts 1990) show that L1457 is strongly fragmented into kinematically and spatially distinct clumps. The velocity range of clump velocities covers $\sim$ 10 kms^{-1} while individual clumps only show linewidths of about 2 kms^{-1}. The ^{13}CO(2→1) map used here (Zimmermann 1993; Zimmermann & Stutzki 1993) was taken with the IRAM 30m telescope. It consists of more than 4000 observed positions and reaches linear resolutions of less than 0.004 pc (12″), thus revealing the structure of L1457 at very small scales. This data set is used here.

The high latitude cloud MCLD 126.6 + 24.5 at a distance of 100 pc is another example of a nearby, quiescent cloud. It is located on the border of the Polaris Flare (Heithausen & Corneliussen 1995) and was studied in several molecular tracers (Corneliussen 1996) with the KOSMA 3m telescope. The line ratios found are consistent with shocked gas being compressed by the North Celestial Pole HI Loop. Here we analyze the cloud structure using ^{12}CO(2→1) emission line data.

The molecular cloud to the north of the H II region NGC 1499 (Herbertz et al. 1991), at the northern boundary of the Perseus OB2 association, does not show evidence of embedded star formation either. It stands out as a particularly turbulent cloud in the Columbia CO survey of dark clouds in Perseus, Taurus, and Auriga (Ungerechts & Thaddeus 1987). Here we will discuss the large scale distribution of ^{13}CO(1→0) emission in the south-western part of NGC 1499 observed with the Nagoya 4m telescope (Herbertz 1992).

S140 is another dark cloud associated with a H II region. The molecular cloud displays the typical signatures of star formation: deeply embedded young B-stars, H_2O masers, and a strong molecular outflow have been found. Its C^{18}O(2→1) emission was observed with the IRAM 30m telescope leading to a linear resolution of 0.05 pc at the distance of 910 pc (Johnen 1992).

The molecular cloud associated with the H II region NGC 7538 is a well known region of massive star formation; a number of O-stars, ultra compact H II regions, masers, and molecular outflows have been found. Here we will use the C^{18}O and ^{13}CO(1→0) maps observed with the 15 element focal plane array receiver at the FCRAO 15m telescope (Röhrig et al. 1995, Röhrig 1996). These large maps consist of more than 2500 positions and cover more than 180 pc^2 with a spatial resolution of 0.5 pc.

The molecular cloud L1630 associated with the Orion B H II region NGC 2024, the reflection nebula NGC 2023, and the optical nebula IC434 is yet another example of a giant molecular cloud actively forming massive stars. Kramer et al. (1996) analyzed its structure by applying the GAUSSCLUMPS algorithm to the large scale distribution of the ^{13}CO(2→1) emission measured with the KOSMA 3m telescope.

M17 SW is a typical giant molecular cloud core lying adjacent to a prominent H II region, which compresses the molecular material and triggers the formation of the next generation of stars. Stutzki & Güsten (1990) describe its structure by analyzing the C^{18}O(2→1) emission with the help of the GAUSSCLUMPS algorithm they developed. The observations were carried out with the IRAM 30m telescope.

Table 1 summarizes the most important observational parameters of the data sets used for the structural analysis. The observations are listed by increasing linear resolutions which range over two orders of magnitude from 0.004 pc to 0.5 pc. Note that most of the clouds were observed on a grid sampled at half the FWHM of the beam. Though not strictly fully sampled according to the Nyquist theorem, that close a sampling is usually regarded as good enough to include most of the spatial information obtainable with the given resolution of the beam. The datasets of Orion B-S, NGC 1499 SW, and MCLD 126.6 + 24.5 were resampled on this finer grid as a preparation for the structural analysis.

Care was taken to avoid that possible calibration gain variations lead to artificial structure in the data. We therefore ignored spectra taken under unstable weather conditions and spectra with doubtful baselines. In general, we subtracted baselines of order $1-3$ from the raw data. The relative calibration accuracy was checked by observing a reference position within each cloud in regular intervals of about one hour. The variation of integrated intensities of these spectra was typically found to be about 10%, slightly higher at the higher frequencies. If possible, this information was used to try to correct the data. In addition, in the case of S140 and L1457 gain variations were at least partly corrected by observing each field of $40'' \times 40''$ with 4 interleaving submaps of 3×3 positions on a 15″ grid sucessively shifted by 7.5″. This method allows to detect drifts and correct for them (Johnen 1992). For a more detailed description of the observations we refer to the references of each data set given above.

3. Clump fitting

3.1. Description of the algorithm

Here we will shortly repeat the basics of the GAUSSCLUMPS algorithm, which was already introduced by SG90. We will concentrate on the parts which influence the number and mass distribution of clumps found. The GAUSSCLUMPS procedure decomposes the observed three dimensional intensity distribution into the emission of individual, Gaussian shaped clumps by iteratively subtracting fitted clumps.

3.1.1. The iteration steps

During the first step of the iterations the algorithm selects the absolute intensity maximum of the observed map and fits a Gaussian shaped three dimensional clump to the surrounding region of the maximum. The fit minimizes a generalized function χ^2 by varying the 10 parameters characterizing a clump. The parameters of a clump are: the position $x_{0,j=1,2}$,v_0 of the clump maximum, its peak intensity a_0, its spatial - and velocity FWHMs along the two principal axes, Δx_j, Δv, the orientation

of the first principal axis, the velocity gradient in both directions and a constant background temperature. The widths of a fitted clump are expressed by

$$\Delta x_j^2 = \Delta_{beam}^2 + \Delta\xi_j^2 \quad \text{and} \quad \Delta v^2 = \Delta_{res}^2 + \Delta\xi_v^2. \tag{1}$$

Here $\Delta\xi_v$ and $\Delta\xi_j$ are the intrinsic, deconvolved clump widths smeared out to the fitted clump width by the limited angular and spectral resolutions Δ_{beam} and Δ_{res}. The fit varies the intrinsic clump widths, so that the fitted clumps are forced to have an observed size at least as large as the spatial and velocity resolution. The algorithm subtracts the fitted clump from the original map creating a residual map, which is used as the input map for the next iteration. This iteration selects again the absolute maximum of the new input map, fits, and subtracts the next clump. These steps are repeated until the intensity of all clumps, integrated over the map, equals the integrated intensity of the original map, or until another, user specified, termination criterion is met. At this point, the peak temperature fluctuations of the residual map are typically about 5 times the rms of the data. This is consistent with the pixel statistics shown in Fig. 2.

3.1.2. The function χ^2

The generalized function χ^2 to be minimized, consists of the standard term $\sum w_i(Y_i - Y_i^{fit})^2$ and three additional terms governed by three user supplied stiffness parameters. Here Y_i is the intensity at point i in the three dimensional data cube and Y_i^{fit} is the intensity at point i of the clump being fitted. Intensities are normalized to the 1σ level within the algorithm. The weighting function w_i at point i is a Gaussian introducing a tapered window centered on the map maximum. This prevents the algorithm from fitting a grand total average over a large region of the cloud instead of fitting the small-scale structure. For numerical convenience GAUSSCLUMPS allows to select a cutoff diameter for the weighting function: only points within this diameter are considered by the fitting procedure, thus limiting considerably the number of data points at which χ^2 has to be evaluated, by ignoring those points which have very low weighting factors anyway, and hence speeding up the calculation. The cutoff diameter and the FWHM of the Gaussian weighting function are user supplied parameters.

A first additional term is added to the generalized χ^2 function which increases the χ^2 for all points where the fitted intensity Y_i^{fit} exceeds the measured intensity Y_i : $s_0 \sum w_i \mathscr{F}(x)$ with $x = Y_i^{fit} - Y_i$. The fitting is thus strongly biased to stay below the observed intensity. SG90 used $\mathscr{F}(x) = \exp(x)$. This exponential term, still increasing χ^2 significantly when the fit is already below the observed image, turned out to lead to a preference to fit low intensity clumps. We now use a 'single sided parabola' function, $\mathscr{F}(x) = \left(0 \text{ for } x \le 0; x^2 \text{ for } x > 0\right)$ which leads instead to a preference to fit a clump below but near the maximum, thus improving the fit behavior. The stiffness parameter s_0 is another of the user supplied control parameters.

The second additional term, $s_a(a_0 + b_0 - Y_{max})^2$, with the peak clump intensity a_0 and the constant intensity offset b_0, keeps the peak amplitude of the fitted clump close to the maximum value Y_{max} of the observed map. The stiffness parameter s_c of the third term keeps the center position of the fitted clump close to the position of the map maximum: $s_c \sum (x_{0,j} - x_j^{max})^2 / \Delta_{beam}^2$ and analogue for the velocity. These last two terms prevent the algorithm to walk off into fitting some edge of the observed region by a large clump centered far outside of the observed region, which may happen when the measured emission does not fall off towards the edges of the observed region.

3.1.3. First discussion

The clumps found do not necessarily correspond to the local maxima of the original data cube, except of course for the first couple of brightest clumps. The algorithm developed by Williams et al. (1994) on the other hand, and all clump decomposition based on eye inspection, identify clumps only when they show up as local maxima in the observed data cube. An advantage of GAUSSCLUMPS is, that it can in principle find clumps blending in position and velocity by a priori assuming a Gaussian shaped clump profile. It is however clear that overlapping clumps are difficult to identify in an unambiguous way in any case, and in particular with a limited signal to noise ratio. Especially at the low mass end the individual clumps can thus not be identified without ambiguities due to the noise.

In addition to the influence of noise, poor quality of the data might mislead the algorithm. Baseline ripples, spikes in the spectra, application of wrong, varying calibration factors (e.g. during unstable weather conditions) obviously lead to additional structure, which, if sufficiently strong, might be interpreted as additional clumpiness.

GAUSSCLUMPS will also find artificial small scale clumps in the case that the clumps themselves exhibit irregular, non-Gaussian shapes. Tests with synthesized clumps of constant brightness temperature show that this leads to additional, small clumps found by the algorithm. The clump mass distribution found does however reflect well the original distribution: only the low mass end of the distribution is artificially crowded (SG90).

3.2. An example

We will now describe the application of the GAUSSCLUMPS decomposition procedure on the Orion B-South ^{13}CO(2→1) data set (Kramer et al. 1996). The data had been taken on a fully sampled velocity grid, but only on a half sampled spatial grid. Since GAUSSCLUMPS fits clumps of at least the sizes of the resolutions, the GAUSSCLUMPS algorithm might be fooled into minimizing the χ^2 function of less massive clumps by fitting very narrow clumps having a width of only one pixel in one direction. To avoid this behavior data should therefore be observed on a fully sampled spatial grid or otherwise at least be resampled on this finer grid. We did the latter with the Orion B dataset.

3.2.1. Panel plots of the clump decomposition

Since the algorithm works and selects clumps in the three dimensional space spanned by the two spatial - and the spectral coordinates, it is not easy to visualize its performance. In Fig. 1 we show the decomposition of the emission into clumps by presenting maps of integrated intensities made after each second iteration of the GAUSSCLUMPS algorithm. Step by step the algorithm fits and subtracts Gaussian clumps which tend to correspond with the peaks of integrated intensities. After the first 20 iterations, the map of the integrated intensities of the 20 identified clumps, which constitute 49% of the total integrated intensity, already shows the main features of the original map. The remaining residual emission still shows peaks far above the noise level, at about 20σ (Fig.1 b20), allowing the algorithm to proceed with the decomposition into clumps.

3.2.2. Influence of the control parameters

We will now discuss the selection of control parameters by presenting criteria to check the reliability of the decomposition algorithm. To this end we varied the stiffness parameters s_0, s_a, s_c and kept the width and cutoff diameters of the weighting function w fixed at 3 times the spatial resolution. In a second step we varied the width of the weighting function while keeping the stiffness parameters fixed to the best values found before.

The stiffness parameters: pixel statistics. Fig. 2a shows histograms of the number of pixels found per temperature interval of the measured map, and of residual maps created by GAUSSCLUMPS after subtracting all clumps found (N_{tot}, see Table 2). This is the fastest way of checking the influence of different stiffness parameter values. The distribution of measured pixels is, of course, asymmetric: the wing at positive brightness temperatures contains the positive signal corresponding to the cloud, in addition to the noise. The wing with negative brightness temperatures should represent the purely Gaussian noise of the observations. After subtraction of all clumps, the corresponding distribution of residual pixels at negative *and* positive temperatures, should also resemble the purely Gaussian noise of the observations.

The width of a Gaussian fitted to the distribution of measured pixels (Fig. 2a) at negative temperatures is $\sigma_{\mathtt{meas}}$ = 0.27 K, which is slightly larger than the average rms temperature of the spectra outside the region of line emission. This is due to slightly varying rms temperatures in the original map.

The histograms of the residual data (Fig. 2a), after the complete decomposition into Gaussian clumps, resemble Gaussian distributions, although they differ in details. Fig. 2b-d show the difference between pixel distributions and a fitted Gaussian function. *At negative temperatures* additional pixels show up above the original Gaussian noise distribution. These are created by two effects: (1) The subtraction of the clumps which all have positive temperatures leads to an enhancement of the negative noise peaks in the residual plots. (2) In addition, the subtraction of third order baselines, which partly lie slightly above the noise of spectral line wings leads to the same feature. The latter point is relevant only for very few spectra of slightly doubtful baselines. The first point does not influence the pixel statistics at positive temperatures, i.e. those pixels which are decomposed to clumps. This argument shows that the feature is of negligible influence for the following discussion of the clump decomposition.

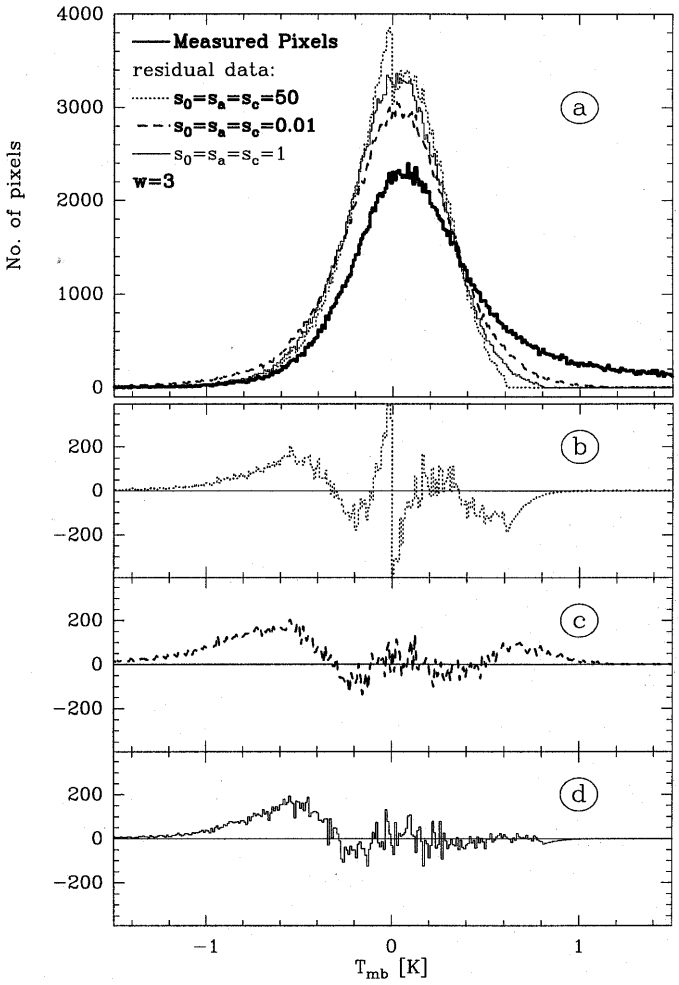

Fig. 2. a The number of pixels per temperature interval is shown for the measured data set and for several residual maps created by GAUSSCLUMPS for different settings of the stiffness parameters. **b-d** The three lower boxes show the difference between the pixel distributions and a Gaussian function fitted to the distributions of the residual data. (The Gaussian was fitted varying its amplitude, center position, and FWHM.)

Deviations from a Gaussian distribution *at positive temperatures*, indicate that GAUSSCLUMPS did not work perfectly well. In this case GAUSSCLUMPS either did not decompose all emission above the noise into clumps or, worse, it decomposed noise peaks into clumps. Especially the latter case has to be avoided by selecting the appropriate stiffness parameters controlling GAUSSCLUMPS.

The maximum temperatures found in the residual distributions (see Fig. 2a) increase with weaker stiffness parameters

from 0.6 K for parameters of 50 to more than 1 K for parameters of 0.01. Due to the subtraction of the clumps, pixels are shifted from positive temperatures to negative temperatures: the number of points with temperatures at e.g. 0 K rises. The 'stiffer' the parameters are, the more points are shifted to low temperatures. At a value of 50 for the stiffness parameters, these pixels become clearly visible as a spike right below zero brightness temperature. The latter signifies that noise peaks were transformed into clumps, a case which is to be avoided.

The best fit of a Gaussian to the residual distribution (Fig. 2d) is achieved for the straightforward selection of stiffness parameters $s_0 = s_a = s_c = 1$. In this case there is barely any difference between the distribution of pixels of the residual map at positive temperatures and a Gaussian fitted to the residual distribution. Also, the width of the Gaussian is $\sigma_{\tt res} = 0.25$ K, very similar to the rms temperature of the original data. When the stiffness parameters are selected much lower ($s_0 = s_a = s_c = 0.01$), emission above this Gaussian noise is left over, i.e. not all emission above the Gaussian noise is decomposed into clumps, as can be seen clearly in Fig. 2c. On the other hand, noise peaks are interpreted as clumps when the stiffness parameters are much larger, i.e. too "stiff" ($s_0 = s_a = s_c = 50$), as can be seen in Fig. 2b. Below we will show that the latter is also the case when the width of the weighting function of χ^2 is selected too narrow.

The stiffness parameters: mass distributions. It is up to the user to decide which of the clumps initially found by the algorithm to use for the subsequent analysis of e.g. the clump mass distribution. The reliable part of the clumps found is conservatively considered here to be restricted to clumps *intrinsically* (Eq. 1) larger than $S = 50\%$ of the resolutions in all three dimensions. We will show below that the high mass part of the clump mass spectrum does not depend on this selection.

The number of thus selected clumps N_{sel} (see Table 2) varies only slightly for stiffness parameter values above 0.1. For stiffness parameters between 0.1 and 10, the discarded clumps contribute only a small fraction of the overall mass of the observed region, although their number is high.

In our example (Table 2), the summed mass of all selected clumps exceeds the mass of the original data set when the values of the stiffness parameters are too low. In the case that s_a is too low, the peak amplitude of the fitted clumps may rise above the maximum value of the observed emission, leading to high clump masses. Broad, extended clumps may be fitted to two or more neighboring local maxima when s_0 is too low, and massive clumps far outside the observed region may be fitted when s_c is too low. The distribution described in row 1 of Table 2 offers an example of this effect. One of the clumps of the ensemble was fitted by a large, very massive clump centered far outside of the map boundaries.

For an optically thin line the mass is proportional to the peak clump intensity times the clump velocity width times the spatial FWHMs along both two principal axes:

$$M \propto T_{pk} \Delta v \Delta x_1 \Delta x_2. \quad (2)$$

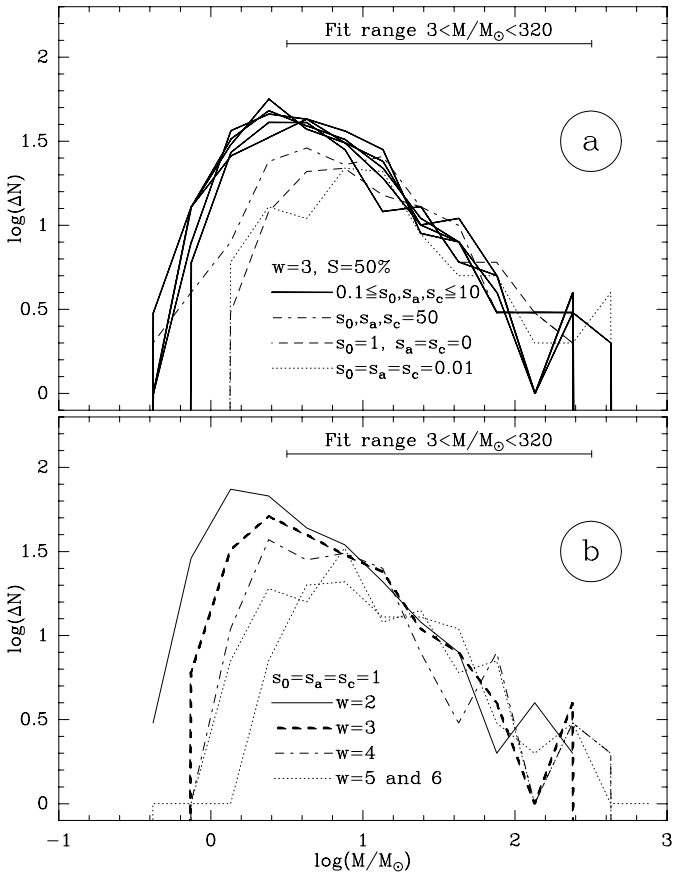

Fig. 3. a Mass spectra of the selected clumps in Orion B found by GAUSSCLUMPS for different values of the user selected stiffness parameters s_0, s_a, s_c. The results of the fit within the selected mass range are given in Table 2. **b** Mass spectra of the clumps in Orion B found by GAUSSCLUMPS for different values of the user selected FWHM of the weighting function w given as a multiple of the resolution. The stiffness parameters were held fixed at $s_0 = s_a = s_c = 1$. Only clumps intrinsically larger than $S = 50\%$ of the resolutions were taken into account.

The proportionality also holds for the optically thick ^{12}CO, for which conversion factors X from integrated intensities to H_2 column densities are given in the literature, although the applicability of these factors to individual clumps may be questionable. For the ^{12}CO(2→1) data of MCLD 126.6 + 24.5 Corneliussen (1996) derived a factor 0.24×10^{20} cm^{-2}/Kkms^{-1}.

The weak contribution of the small clumps to the overall mass is reflected by the power law distribution of clump masses: The number of clumps per mass interval was fitted by a power law $dN/dM \propto M^{-\alpha}$ in the mass range $3 < M/M_\odot < 320$ assuming errors for each mass bin to be equal to $\sqrt{N}$. Fig. 3 shows the clump mass spectra of the distributions given in Table 2. The mass distributions for different values of the stiffness parameters between 0.1 and 10 are well fitted (Table 2) by the above power law distribution. In addition, the spectral index is nearly constant with $\alpha = 1.72 \pm 0.05$. The statistical scatter in the individual mass distributions is larger, $\sigma = 0.09$, than the scatter due to different input parameters: $1.65 < \alpha < 1.76$.

Table 2. Results of the GAUSSCLUMPS algorithm applied on the Orion B dataset for different values of the user supplied stiffness parameters s_0, s_a, s_c, and different widths of the weighting function w in units of the resolutions. The cutoff width of this function always is a factor of $2-3$ larger. The algorithm always terminated when the integrated intensity of the residual map was about to fall below zero. N_{tot} is the total number of clumps found by the algorithm. N_{sel} is the number of clumps larger than 50% of the resolutions in all three dimensions. Column (7) gives the percentage of the number of clumps fulfilling this criteria. The total mass of the selected clumps and the percentage relative to the original integrated intensity which corresponds to 3700 $M_\odot$, are given in columns (8) and (9). The spectral index and the correlation coefficient resulting from a linear least squares fit of the function $\log N = (1-\alpha)\log(M/M_\odot) + \log N_0$ ($\Leftrightarrow N = N_0 M^{1-\alpha} \Leftrightarrow dN/dM = N_0(1-\alpha)M^{-\alpha}$) to the binned data over the mass range $1 < M/M_\odot < 320$ are shown in the last two columns.

s_0 (1)	s_a (2)	s_c (3)	w (4)	N_{tot} (5)	N_{sel} (6)	(7)	$M_{tot}/M_\odot$ (8)	(9)	α (10)	r (11)
1	0	0	3	236	107	(45%)	$4.5\,10^5$	-	1.54	−0.95
0.01	0.01	0.01	3	219	100	(45%)	3632	(98%)	1.54	−0.77
0.1	0.1	0.1	3	585	185	(31%)	3194	(86%)	1.75	−0.97
1	1	1	3	879	216	(24%)	2970	(80%)	1.72	−0.96
5	1	1	3	1003	218	(22%)	2976	(80%)	1.65	−0.96
5	5	5	3	1181	217	(18%)	2838	(77%)	1.73	−0.98
10	10	10	3	1564	206	(13%)	2798	(76%)	1.76	−0.99
50	50	50	3	3067	147	(5%)	2516	(68%)	1.60	−0.91
1	1	1	2	1313	302	(23%)	2784	(75%)	1.78	−0.98
1	1	1	3	879	216	(24%)	2970	(80%)	1.72	−0.96
1	1	1	4	501	158	(32%)	3242	(88%)	1.62	−0.87
1	1	1	5	349	122	(35%)	3400	(92%)	1.54	−0.79
1	1	1	6	251	97	(39%)	3470	(94%)	1.48	−0.89

The weighting function. The width of the Gaussian function weighting the observed points in the surrounding of a clump peak (see §3.1.2), is another of the user supplied control parameters. The weighting is used to bias the algorithm to fit individual clumps instead of an average, smeared-out, broad clump. The latter happens when the width of this function is too broad. A small width does however not imply a maximum possible clump size, it merely introduces a bias to fit the small-scale structure in case it is present.

Table 2 and Fig. 3b clearly show the influence of different widths on the number of clumps found and on the clump mass spectrum when the stiffness parameters are fixed at the optimum values found above. The spectral index for clump masses $M >$ 10 $M_\odot$ stays nearly constant, although there is a tendency to more shallow distributions for larger widths. The number of low mass clumps rises with decreasing widths of the weighting Gaussian.

Care has to be taken when interpreting the results of the figure. Although the best fit, i.e. a fit giving a linear mass spectrum in a log-log plot over the largest range of masses, is achieved for w = 2 or less, a look at the corresponding histograms of the residual data reveals that noise peaks were interpreted as clumps similar to what is seen in Fig.2b. This means that the width was selected too narrow.

We conclude that a width of the weighting function of about 3 times the resolutions gives the best overall results with α = 1.72 and a linear correlation coefficient of $r = -0.96$ over the range $3 \leq M/M_\odot \leq 320$. As long as the cutoff width of the weighting function, introduced in §3.1.2, it is at least a factor of two to three larger than the chosen FWHM, it has no influence on the distributions.

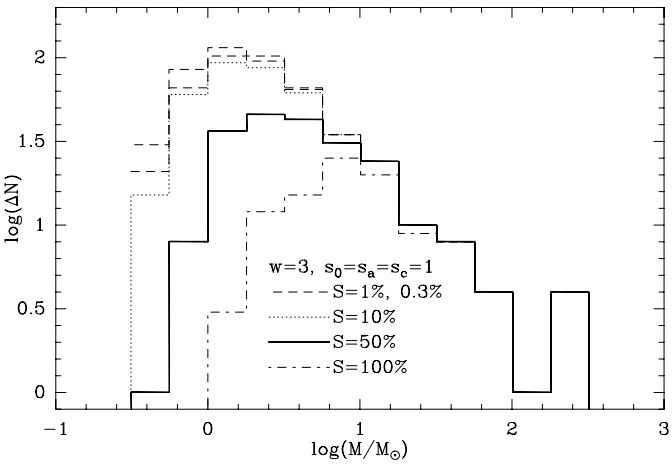

Fig. 4. Mass spectra of clumps selected with respect to their size from the clumps decomposed by GAUSSCLUMPS. Only clumps with intrinsic widths of at least $S\%$ of the resolution limits in all three dimensions are selected.

Influence of the size selection. Given the above criteria for the selection of parameters, which are of course to some extent specific to the Orion B data set, we find that the parameter settings $s_0 = s_a = s_c = 1, w = 3$ give the most reliable results. We had conservatively selected clumps from the output of GAUSSCLUMPS which have intrinsic widths of a least S = 50%

of the resolutions in all three dimensions. In this case 80% of the total mass was deconvolved into clumps and selected for the mass spectra. These clumps constitute only 24% of all clumps originally found by GAUSSCLUMPS (Table 2).

Fig. 4 shows the influence of different selection limits. The high mass part ($M > 6$ M$_\odot$) of the mass distributions barely changes when applying different limits. Given the power law distribution, it is thus clear that the overall mass of all clumps barely changes, while the number of clumps may change significantly. When selecting only clumps intrinsically larger than 10% of the resolutions, the selected clumps constitute 89% of the total mass and 46% of all clumps originally found. The positions of these discarded clumps are evenly distributed in all three dimensions. Although the data is fully sampled, it is thus clear that GAUSSCLUMPS often fits intrinsically very small clumps of low mass; the distribution of clump masses is only influenced at the low mass end.

These very small clumps might be artificial features unlikely to represent real physical entities as was already noted by SG90 and Hobson et al. (1994). They too, excluded 'doubtful' clumps, with dimensions at the beam size and velocity resolution, from further analysis. On the other hand there is no a priori reason why the observed clouds should not contain a larger and larger number of smaller and smaller clumps. One should note that lowering the cutoff criterion for including smaller clumps into the mass spectrum, in all cases presented, simply fills in the small mass end of the power law mass spectrum. Speculation about the 'reality' of these small clumps is obsolete; only higher resolution observations with higher S/N can definitely show whether the mass spectrum continues down to smaller clumps.

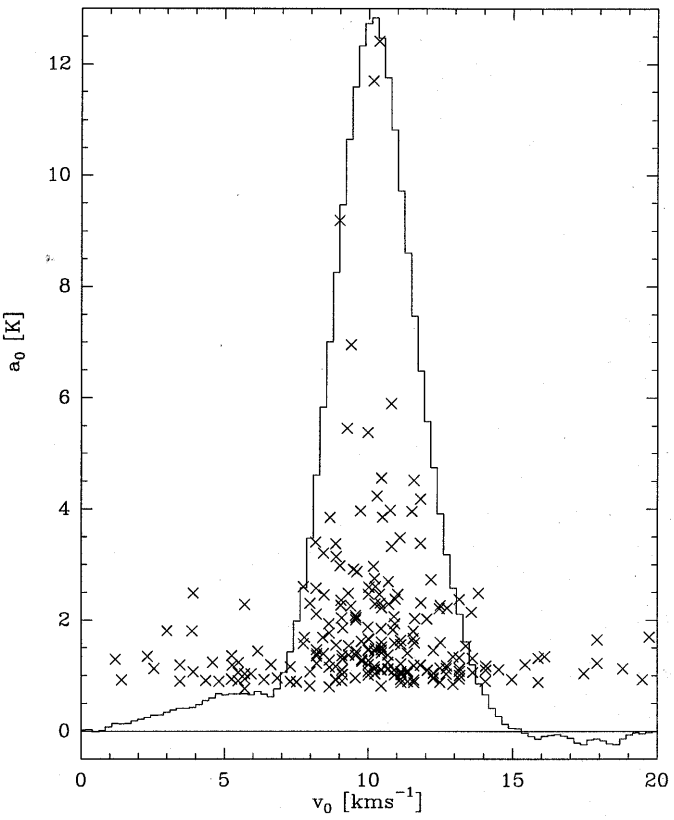

Fig. 5. Velocity of clump maximum v_0 and peak intensity a_0 of all 216 selected clumps ($s_0 = s_a = s_c = 1, w = 3, S = 50\%$). Overlayed is the positional average of all ^{13}CO(2→1) Orion B spectra. (Temperatures of the spectrum are multiplied by 5, the peak temperature is 2.6 K).

3.2.3. The distribution of clump velocities and temperatures

One more way to test the performance of the algorithm for a given set of control parameters ($s_0 = s_a = s_c = 1, w = 3, S = 50\%$) is shown in Fig. 5. It presents, for each of the 216 selected clumps, the clump center velocity and peak temperature. Superimposed is a spectrum of the averaged ^{13}CO(2→1) emission. All clumps show peak temperatures significantly above the general noise level, $a_0 \geq 0.8 = 3\times$rms. In addition, the center velocities of 206 clumps, out of 216 identified, lie in the velocity range of emission. A few spectra in the north of the region mapped show ripples in the velocity range 15 to 20 kms^{-1} outside the region of emission. These show up as 10 additional, artificial clumps in Fig. 5. The clumps at velocities of $v \lesssim 5$ kms^{-1} belong to an emission component in the north-east described in Kramer et al. (1996).

This is one additional proof, that almost all clumps, in this case $\sim 95\%$, are decomposed from the emission and not from noise peaks.

3.2.4. The lower mass limit

The minimum possible mass is given by the spatial and velocity resolution, and the rms noise of the data. This is the least massive clump mass the GAUSSCLUMPS algorithm can possibly find (cf. Eq. 1). For the Orion B data this gives

$$M_{min}^{limits} \propto T_{rms}\Delta_{res}\Delta_{beam}^2 = 0.056 \quad \mathrm{M}_\odot. \tag{3}$$

The smallest clump masses M_{min}^{cl} of the distributions described above always is higher by a factor of at least a few than this minimum possible mass.

The smallest clump mass of the most reliable distribution (see above) is 0.52 M$_\odot$. Its peak intensity is $a_0 = 0.92$ K, and the widths are $\Delta x_1 = 2.58'$, $\Delta x_2 = 2.58'$, $\Delta v = 0.54$ kms^{-1}. This mass is a factor of 9 larger than M_{min}^{limits}. The velocity of the clump maximum is 11.6 kms^{-1}, at the center of line emission in Orion B.

The clump masses are determined to a high accuracy, since the mass of a clump is an integral quantity. It does not depend on the exact widths found by GAUSSCLUMPS nor on the actual resolutions in the limit that blending of small clumps into larger clumps can be neglected. If e.g. the intensity fitted to a clump is a bit too high, the fitted width will be a bit too low, and the clump mass will stay constant. This correlation of the individual errors of the parameters shows up in the non-diagonal, negative elements of the error matrix in the least squares fit procedure (e.g. Bevington & Robinson 1992). The determination of the

Table 3. User supplied parameters selected for the Gaussian decomposition of the eight data sets. Only clumps intrinsically larger than the selection limit S in all three dimensions are taken into account for the mass spectra.

	s_0	s_a	s_c	w	S
L1457-S	3	0.1	0.1	3	12%
S140	5	0.1	0.1	2	12%
MCLD 126.6+24.5	5	0.1	0.1	4	32%
M17 SW	1	1.0	1.0	3	12%
Orion B-S	1	1.0	1.0	3	50%
NGC 1499 SW	5	0	0	4.5	26%
NGC 7538 $C^{18}O$	5	0.1	0.1	4	26%
NGC 7538 ^{13}CO	5	0.1	0.1	3	26%

clump mass therefore is intrinsically much more accurate than the determination of e.g. a clump radius or clump line width.

In addition, the above discussion shows that even the least massive clump found, is significantly more massive than the minimum clump mass given by the observational limits. This holds as well for the other data sets discussed below (Table 4).

4. Results

4.1. Mass spectra of the seven clouds

We applied the GAUSSCLUMPS algorithm to our data sets of the seven molecular clouds L1457-S, MCLD 126.6+24.5, S140, M17 SW, Orion B-S, NGC 1499 SW, and NGC 7538 presented in §2.

For each data set we used a set of control parameters (Table 3) which leads to the most reliable distribution of clump masses. For this, we followed the recommendations given above for the Orion B data set. In particular, histograms of the number of pixels per temperature interval (Fig. 2) were created to verify that the algorithm fits clumps above the noise limits.

Here we will focus on the resulting clump mass spectra which are shown in Fig. 6 (Table 4). Like in the case of the Orion B data set, even the smallest clump masses are significantly larger (3 to 13 times) than the minimum possible mass given by the observational limits (Eq. 3, Table 1).

The range of clump masses covers more than seven orders of magnitude, $2 \times 10^{-4} \leq M/\mathrm{M}_\odot \leq 10^4$, thereby significantly improving upon earlier studies which do not reach masses that low. The least massive clumps found in the nearby, quiescent clouds L1457 and MCLD are unambiguously sub-stellar some of them as low as a third of the mass of Jupiter. They have radii of down to 10^{-3} pc ($\sim$ 200 AU). In contrast, the giant molecular clouds M17 SW and NGC 7538, currently forming massive stars, exhibit clumps as massive as 10^4 $\mathrm{M}_\odot$ and as large as 0.6 pc.

The spatial dynamic range, defined as the ratio of mapped area to resolution (Table 4), is reflected by the number of clumps found within each mapped region: the clump number ranges between 10^2 and more than 10^3. These numbers, obviously, are also influenced by the spectral dynamic ratio of line width over spectral resolution and by the signal-to-noise ratio of the observations (Table 1).

All mass distributions are well fitted by a power law function $dN/dM \propto M^{-\alpha}$ over the clump mass ranges of the individual clouds (Table 4) with spectral exponents α varying between 1.6 and 1.8, and an average value of $\alpha = 1.69 \pm 0.06$. Here dN/dM is the number of clumps per solar mass interval. The constancy of the spectral index is rather surprising given the large range of clump masses covered and the differences in physical conditions between the individual clouds observed. In addition, the spectral index appears to be independent of possible optical depth effects dependent on the CO isotopomer used.

Neither of the seven clouds shows indications of a systematic change of the power law exponent for different clump masses over the fitted regions.

The only distinguishing features of the clump mass spectra of the various sources (Fig. 6) are the 'turnover' of the mass spectra at the low mass end, the maximum clump mass found, and their total number of clumps. The turnover at the low mass ends always lies a factor of only 1.5 to 6 above the smallest clump mass identified, M^{cl}_{min} (Table 4). This turnover is influenced by the resolution and noise limits and by how the GAUSSCLUMPS algorithm works. The turnover does therefore not reflect a real change of the power law exponent.

The way the clump identification works, the maximum clump masses found reflect the peak temperatures, maximum line widths, and largest spatial clump sizes found in an observed region. Giant molecular clouds with ongoing star formation like Orion B-S exhibit massive clumps of up to several 10^2 $\mathrm{M}_\odot$, whereas quiescent, cold clouds like NGC 1499 SW, at nearly the same distance and with similar resolutions, only show clumps of less than several 10 $\mathrm{M}_\odot$ (Table 4). The observations of L1457-S (Zimmermann 1993) and other clouds (e.g. Langer et al. 1995) have shown that the spatial - and also the spectral structure breaks up into smaller units when observing at higher resolutions. This indicates that the most massive clumps found in our analysis might well consist of substructure blended together by our limited spatial resolutions and possibly by having similar velocities leading to overlapping emission lines along the line of sight. One should note, however, that the cloud mass is dominated by the few most massive clumps identified. This is because the spectral index of the mass spectra is $\alpha < 2$. The break up of a massive clump into substructure at higher resolution will thus mostly add many more lower mass clumps, but will only decrease slightly the mass of the massive, blended clump identified originally at lower resolution.

4.2. Comparison with results from the literature

Similar power-law exponents for the mass range $1 < M/\mathrm{M}_\odot < 10^7$ have been found in a number of studies of interstellar clouds comprising a variety of clouds and also a variety of at least four different clump finding techniques. The mass spectra of dark clouds and giant molecular clouds in the first and second galactic quadrant were analyzed by Casoli et al. (1984,

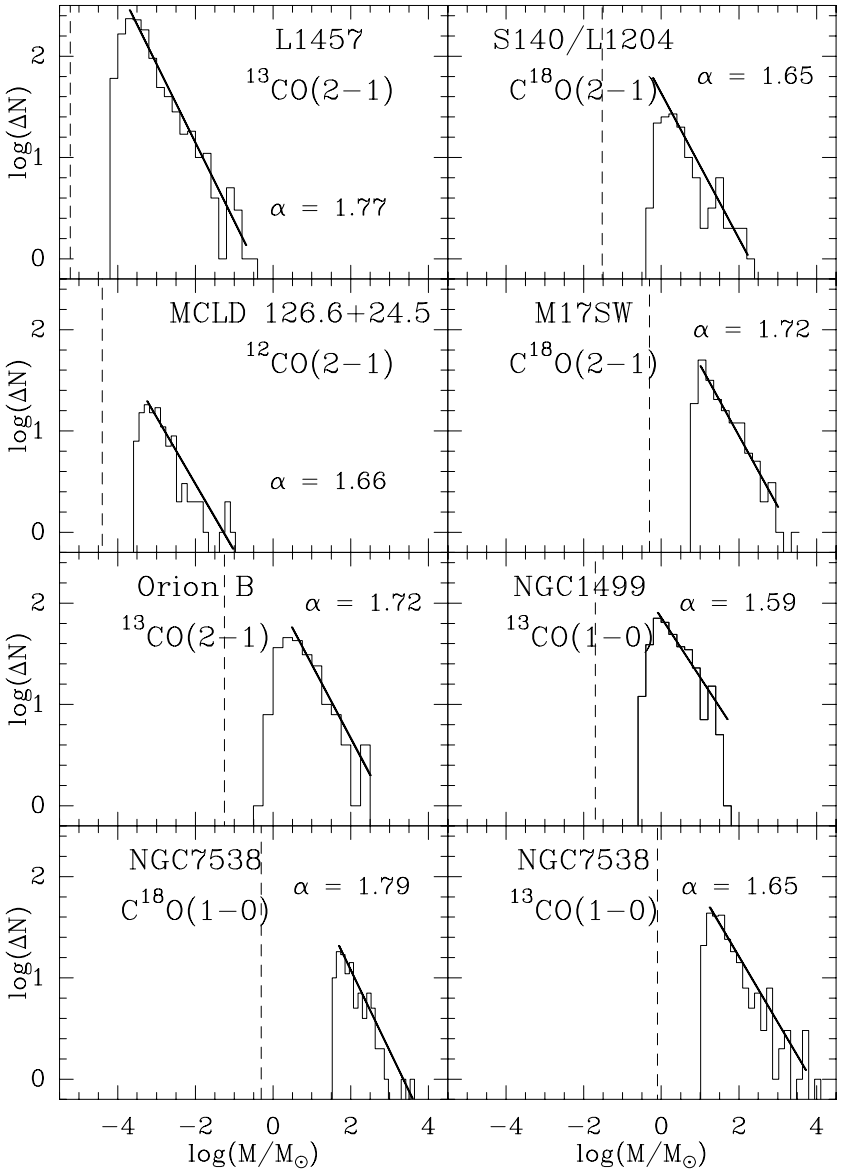

Fig. 6. Clump mass spectra of the eight data sets we analyzed. All spectra are fitted by a power law function $dN/dM \propto M^{-\alpha}$. The straight line represents the best linear fit over the range of masses spanned by the line. The resulting indices α lie in the range 1.59 to 1.79. The minimum possible mass M_{min}^{limits}, given by the resolution limits and the rms noise, is denoted by a dashed line for each data set.

Table 4. The results of the eight surveys ordered by increasing spatial resolution. The solar distance, the spatial resolution, and the area covered by the surveys are given in columns (1,2,3). The spatial dynamic range, area/HPBW^2, and the number of selected clumps, are presented in columns (4) and (5). The total mass of all clumps selected and the minimum mass detectable due to the finite resolutions are given in columns (6) and (7). The next column (8) gives the smallest clump mass of the distribution. Columns (9) and (10) show the mass range used for the least squares fit of the function $N = N_0 M^{1-\alpha}$. The last column (11) gives the fitted spectral index α.

	D	HPBW	area	d.r.	N_{sel}	M_{tot}	M_{min}^{limits}	M_{min}^{cl}	mass range		α
	[pc]	[pc]	[pc^2]			[M$_\odot$]	[M$_\odot$]	[M$_\odot$]	[M$_\odot$]	[M$_\odot$]	
	(1)	(2)	(3)	(4)	(5)	(6)	(7)	(8)	(9)	(10)	(11)
L1457-S	65	0.004	0.022	1375	1306	2.65	0.06 10^{-4}	0.6 10^{-4}	2 10^{-4}	0.2	1.77±0.30
S140	910	0.057	1.208	372	130	840	0.03	0.4	0.6	160	1.65±0.18
MCLD 126.6+24.5	100	0.061	0.710	194	117	0.638	0.4 10^{-4}	3 10^{-4}	6 10^{-4}	0.09	1.66±0.10
M17 SW	2200	0.139	2.458	127	179	13000	0.5	5.6	10	1000	1.72±0.15
Orion B-S	400	0.242	35.500	606	216	2970	0.06	0.52	3	320	1.72±0.09
NGC 1499 SW	350	0.305	124.500	1335	357	1303	0.02	0.25	0.8	50	1.59±0.06
NGC 7538 C^{18}O	2200	0.533	179.200	630	110	27000	0.5	34	50	3900	1.79±0.12
NGC 7538 ^{13}CO	2200	0.533	264.500	931	246	56000	0.8	10	17	10700	1.65±0.05

300 clouds, $1.45 < \alpha < 1.6$, $10 < M/\mathrm{M}_\odot < 10^5$), Sanders et al. (1985), and by Solomon & Rivolo (1989, α = 1.5, 440 clouds, $3 \times 10^5 < M/\mathrm{M}_\odot < 4 \times 10^6$). See also the review of Scalo (1985). Dobashi et al. (1996) recently analyzed the mass spectrum of 159 isolated molecular clouds in the Cygnus region which were observed in ^{13}CO(1→0). They find an index of 1.6 for cloud masses between 10^2 $\mathrm{M}_\odot$ and 10^5 $\mathrm{M}_\odot$. The mass spectrum of 112 massive clouds of the outer Galaxy has an index of 1.62 (Brand & Wouterloot 1995) over a range of cloud masses $4 \times 10^4 \leq M/\mathrm{M}_\odot < 8 \times 10^6$. Similar indices were found by analyzing ^{13}CO(1→0) data of Cepheus OB3 (Carr 1987, α = 1.4 computed by Blitz 1993) and of ρOphiuchus (Loren 1989, α = 1.7 recomputed and corrected by Blitz 1993). Nozawa et al. (1991) derived the same index from their ^{13}CO study of ρOphiuchus. Observations of the distribution of CS emission in the Orion A and B clouds both lead to a power law exponent of α = 1.6 (Tatematsu et al. 1993; Lada et al. 1991a).

While all the above studies are based on eye-inspections, there are a few studies based on automated algorithms, although comprising only less than 10^2 clumps. Langer et al. (1993) used wavelets (Laplacian pyramid transforms) to analyze the structure of the cold dark cloud B5 as seen in velocity integrated ^{12}CO emission. They derived a spectral index of α = 1.68 for the 58 clumps identified. The GAUSSCLUMPS algorithm was applied to HCO^+, HCN, and $C^{17}O$ maps of a part of M17 SW (Hobson 1992, Hobson et al. 1994) leading to the identification of 19 to 35 clumps depending on the tracer, following a power law with α = 1.9. We note that the spatial dynamic range of these data sets is only $\sim$ 70, which is reflected by the low number of clumps found.

Williams et al. (1994; 1995) used their clump finding algorithm to determine the structure of the Maddalena - and of the Rosette cloud from ^{13}CO(1→0) data. They find rather shallow mass distributions with α = 1.44 in the case of Maddalena and α = 1.27 in the case of Rosette. The number of clumps identified is 43 and 70 respectively. We already sketched the working of this algorithm in the introduction. Similar to all methods based on eye-inspection, it identifies all clumps with local maxima in the original map. It thus cannot find less massive clumps which are blended by others. Therefore, the low mass clumps are largely missed, the range of clump masses is more restricted as compared to the results of the GAUSSCLUMPS algorithm. In addition, low mass clumps are coadded to the more massive clumps, therefore leading to more shallow mass spectra. This restriction does not apply to those investigations, which analyze the mass spectrum of a sample of individual clumps or clouds, which have no apparent connection to each other at the noise level (e.g. Casoli et al. 1984; Brand & Wouterloot 1995; Dobashi et al. 1996).

The exponent derived in the different studies lies in the range $1.4 \leq \alpha \leq 2.0$. Our observations double the number of individual clouds analyzed with high dynamic ranges, delivering additional strong evidence for a common spectral index of about 1.65 ± 0.1 for all molecular clouds. Including the studies of Giant Molecular Clouds, the spectral index appears to be nearly constant over about 10 orders of magnitude in clump and cloud masses. There are no indications of a characteristic clump mass. In contrast, Pound & Blitz (1995) recently discussed indications for fewer low-mass ($M < 0.1$ $\mathrm{M}_\odot$) clumps than expected from any known mass spectrum, by analyzing $C^{34}S$ and DCO^+ molecular line data of Ophiuchus and Taurus. These molecules are however tracers of high volume densities and as such do not necessarily trace H_2 column densities and masses.

For neither of our seven samples do we find indications of a flattening of the distribution with decreasing clump mass like seen in the mass spectrum of CS clumps in Orion A (Tatematsu et al. 1993). A flattening is predicted by the work of Das & Jog (1996), who performed numerical N-body and hydrodynamic simulations of gravitationally interacting and colliding clumps. For masses above a certain value, their computer models evolve however from a random distribution of clouds to a power law distribution of cloud masses with indices between 1.7 and 1.9. These are consistent with observations.

The least massive clumps in L1457 and in MCLD 126.6 + 24.5 are significantly less massive than their corresponding virial masses by factors of 100 to 1000 (Zimmermann 1993, Corneliussen 1996), and therefore well beyond gravitational influence. We do not find any bound clumps at all in these two clouds, although the more massive clumps are closer to being bound than the less-massive ones. There is thus no indication of self-gravitating clumps of sub stellar mass, the putative proto-brown dwarfs. A similar conclusion was drawn by Pound & Blitz (1993, 1995) who studied the small-scale structure of several high-latitude clouds, among them L1457, finding no clear evidence of self-gravitating clumps of any mass in them, although they found clumps with masses as low as 5×10^{-3} $\mathrm{M}_\odot$. In contrast, the most massive clumps in GMCs like M17 SW or Orion B are nearly virialized (SG90, Kramer et al. 1996). A constant clump mass exponent thus appears to be present, independently of the importance of self-gravity. This indicates that, at least the least massive clumps found, do not represent well defined physical entities but instead are likely to be transient features of the turbulent structure dissolving and reforming fast unless supported by external pressure or internal forces. Silk (1995) suggests that rotationally supported low-mass fragments might be long lived enough to retain a large cross section for mutual collisions and grow by coalescence. The Taurus molecular cloud TMC1 (Langer et al. 1995) as well as the quiescent core L1498 (Lemme et al. 1995) show similar small-scale fragmentation. Both studies, using a variety of tracers, find very small clumps with diameters of less than about 0.02 pc and even 0.007 pc in the case of TMC1. The least massive clumps are of the order of 0.01 $\mathrm{M}_\odot$ and show extremely narrow line widths of 0.11 kms^{-1}. Like the low-mass clumps in L1457 decomposed from our ^{13}CO(2→1) dataset, the low-mass clumps in TMC1 and L1498 are gravitationally unbound by a large factor.

5. Discussion

Visual inspection of position-velocity cuts and of channel maps of molecular clouds, indicate a large number of structures; all these maps exhibit a complex, inhomogeneous, nested, filamen-

tary, or clumpy structure on all scales down to the resolution limits. These maps appear self-similar: the structure looks the same independent of the scales. The derivation of clump mass spectra leads to a better quantification of this description. Another motivation to analyze the distribution of clump masses is, that it possibly determines the stellar initial mass function, which in turn determines all stellar evolution, and its links with star formation efficiency (Zinnecker et al. 1993).

The sign and slope of the observed clump mass distribution show that the total number of clumps is dominated by the least massive clumps: $N_{tot} = \int dN = N_0(M_{min}^{1-\alpha} - M_{max}^{1-\alpha})$, where M_{min} and M_{max} are the smallest and largest clump mass found. In addition, the slope implies large numbers of clumps: assuming the most massive clump has 1000 $M_\odot$ and the slope is α = 1.7, then the total number of clumps with $M \geq 0.5 M_\odot$ is 200. Taking this into consideration, the large number of clumps generally found by the GAUSSCLUMPS algorithm is reasonable.

Assuming that our cloud sample is representive for molecular clouds in the galaxy and adding the results of other studies, we find evidence for a common spectral index for all interstellar clouds, whether quiescent or forming massive stars. This implies that the power law exponent probably is invariant to the evolutionary stage of a molecular cloud, indicating a common, time independent mechanism creating the structure within the clouds, as it is seen with column density tracing molecules.

The total cloud mass, $\int NdM$, is proportional to $(M_{max}^{2-\alpha} - M_{min}^{2-\alpha})$. For an exponent α of less than 2, the total mass is therefore determined by the few most massive clumps. In the example of Orion B, the 5 most massive out of 216 clumps found, constitute 35% of the total cloud mass. In contrast, most of the stellar mass in our galaxy is contained in the low mass stars, since the stellar mass distribution is much steeper, α = 2.35 (Salpeter 1955) than the clump mass distribution. Zinnecker et al. (1993) point out that a decrease in efficiency $\propto M^{-1/2}$ in converting clump to star mass might explain this steepening. Protostellar winds, radiation pressure in protostellar envelopes, and magnetic field tension may work together to decrease the efficiency with rising clump mass and physically justify the power ~ -0.5. Alternatively, the most massive clumps might fragment at some moment of their lifetime into a number of less massive star forming pre stellar cores. This would also explain the steepening of the IMF relative to the clump mass spectrum. The near infrared observations of Lada et al. (1991b) in Orion B have indeed shown, that star formation is almost entirely restricted to three of the most massive CS clumps found. The efficiency of star formation increases with core mass from $\sim$ 3% to 30% (Lada 1992). High gas mass is however not a sufficient condition for star formation, as two of the most massive clumps in Orion B show only low levels of star formation activity. Similarly Williams et al. (1995), who compared ^{13}CO clumps in Rosette with IRAS point sources, found that star forming clumps are bound and massive, but that several of the bound, massive clumps are not associated with an IRAS source. The above findings indicate that the massive clumps found in the seven clouds of our study have significant substructure. If these observations can be generalized, then these most massive clumps are the most probable sites of ongoing or future star formation.

Whether the power law clump mass spectrum of a cloud which forms *massive stars* continues below one solar mass, is still unclear. The influence of massive star formation might change the cloud structure and the clump mass distribution at the small scales reached in the quiescent clouds L1457 and MCLD 126.6 + 24.5.

Interestingly, the same scale invariance over a large range, like for the clump mass spectrum, seems to hold for the area-perimeter relation $P \propto A^{D/2}$ of iso-intensity contour lines. Falgarone et al. (1991) find a constant fractal dimension D = 1.36 over the range between 100 pc down to 0.05 pc by analyzing edges of quiescent interstellar clouds in CO. Elmegreen & Falgarone (1997) pointed out recently a possible connection between the fractal dimension, the mass size relation, and the power law index of the cloud mass distribution. Stutzki et al. (1997) show that an ensemble of clumps with a power law mass spectrum and a specific mass size relation results in a column density distribution with fractal characteristics. The power law index of the mass spectrum can thus be viewed as just another measure of the fractal dimension of the cloud image.

6. Summary

We used large scale isotopomeric CO maps of the seven molecular clouds L1457, MCLD 126.6+24.5, NGC 1499 SW, Orion B South, S140, M17 SW, and NGC 7538, to analyze their clumpy structure in terms of the number distribution of clump masses. These were derived by decomposing the emission line data into Gaussian shaped clumps using the GAUSSCLUMPS algorithm developed by Stutzki & Güsten (1990).

We explained the working of this algorithm and discussed the influence of its control variables, taking the Orion B ^{13}CO(2→1) data (Kramer et al. 1996) as an example. A map showing the successive and iterative subtraction of the first 20 Gaussian shaped clumps from the original distribution is presented. The histograms of the number of pixels found per temperature interval of the measured map, and of residual maps, offer the best and easiest way to check that GAUSSCLUMPS does decompose all emission above the Gaussian noise into clumps, without interpreting noise peaks as clumps. The resulting spectra of the clump mass distribution are rather insensitive to the exact values of the user supplied stiffness parameters over a certain range. We discard clumps near the resolution limits as possible artifacts and note that their contribution to the overall mass is small. The user supplied width of the weighting function, which prevents the algorithm from fitting a broad average over several clumps instead of individual clumps, influences the form of the power law mass spectra only at the low mass end. We thus find criteria to check the proper performance of the algorithm. Taking into account the recommendations for the choice of control parameters, we applied GAUSSCLUMPS on the data of the seven molecular clouds.

For all clouds we find power law mass spectra of the form $dN/dM \propto M^{-\alpha}$ with α lying between 1.6 and 1.8. The num-

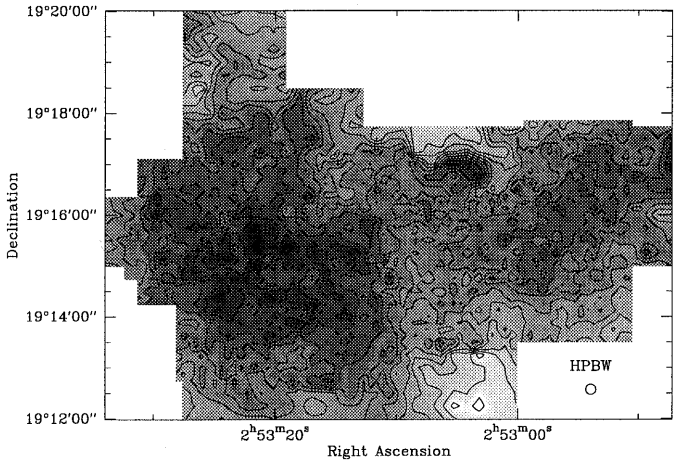

Fig. 7. ^{13}CO(2→1) emission of the southern part of L1457 integrated over the range of emission from −8 to −1 kms^{-1}. Observations were carried out with the IRAM 30m telescope. Contours range from 0.7 (= 3σ) to 15.4 by 1.4 Kkms^{-1} ($\int T_{mb} dv$) (Zimmermann 1993).

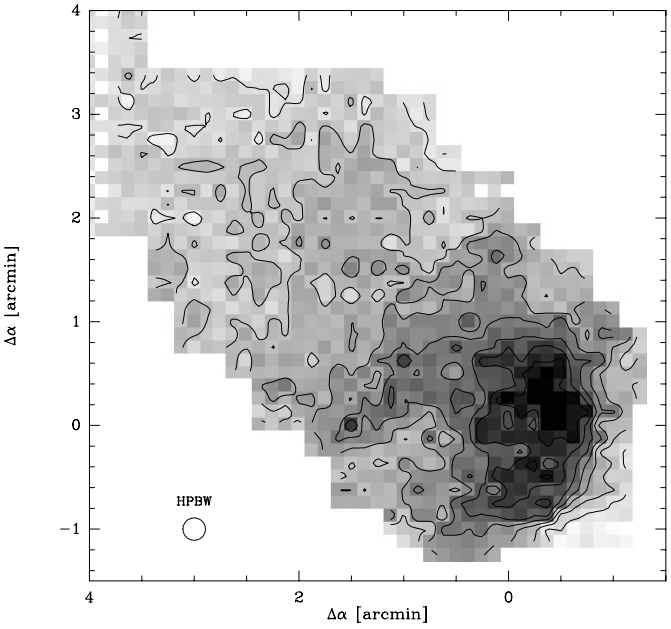

Fig. 8. Velocity integrated C^{18}O(2→1) emission of S140 observed with the IRAM 30m telescope. The coordinate offsets are relative to α_0 = $22^h17^m42^s$, δ_0 = 63°03′45″ (1950). The range of integration is −12 to −3 kms^{-1} and contour levels are from 3.6 (= 3σ) to 28.8 Kkms^{-1} by 3.6 Kkms^{-1} (Johnen 1992).

ber of clumps found in the different clouds lies between 127 and 1375 depending on the dynamic ranges reached by the observations. Due to the different telescopes, observing frequencies, and distances to the clouds, the data cover a wide range of clump masses: $10^{-4} < M/\mathrm{M}_\odot \leq 10^{+4}$. Several investigations of clump and cloud mass spectra are presented in the literature, although there are only few publications which find more than 100 clumps allowing to derive significant results. All these investigations find a common spectral index of about $1.4 \leq \alpha \leq 1.9$ for masses between 1 and 10^7 solar masses. These results agree with our analysis. The sign and slope of the clump mass spectra commonly found, signifies that the total number of clumps is large and dominated by the least massive clumps, while on the other hand, the total mass is dominated by the most massive clumps.

The data of L1457 and MCLD 126.6+24.5, presented here, show for the first time a clear continuation of this common spectral index down to masses of about 10^{-4} M$_\odot$, i.e. to clumps less massive than Jupiter. The spectral index of clumps and clouds within the Galaxis thus seems to be nearly constant with $\alpha = 1.65 \pm 0.1$ over about 10 orders of magnitude in mass. There thus is no indication of a characteristic clump mass. The minimum mass detectable given the resolution limits of the observations, is always near the turnover point of the clump mass spectra, signifying that this turnover point does not present a true change in slope of the clump distribution but instead is due to the under sampling of the clumps of lowest mass.

Since the clumps found in L1457 and MCLD 126.6 + 24.5 are clearly substellar and not virialized by factors of 10 to 1000, the mass spectrum appears to be invariant to the importance of self-gravity.

The molecular clouds analyzed here, cover a wide range of physical conditions: while e.g. L1457 is a small, quiescent cloud without any evidence for star formation, the giant molecular cloud associated with NGC 7538, similar in this respect to Orion B and M17 SW, exhibits all signatures of ongoing formation of massive stars. A constant spectral index of the power law distribution of clump masses for all these different clouds indicates, that the index is invariant to the star formation activity and to the evolutionary stage, i.e. the age, of a molecular cloud or of a whole region of clouds.

Acknowledgements. We acknowledge the helpful comments of an anonymous referee. The KOSMA 3m radio telescope at Gornergrat-Süd Observatory is operated by the University of Cologne and supported by the Deutsche Forschungsgemeinschaft through grant SFB-301, as well as special funding from the Land Nordrhein-Westfalen. The Observatory is administered by the Internationale Stiftung Hochalpine Forschungsstationen Jungfraujoch und Gornergrat, Bern. We would like to thank the Five College Radio Astronomy Observatory for the observing time for NGC 7538. FCRAO is supported in part by the National Science Foundation under grant AST 94-20159 and is operated with permission of the Metropolitan District Commission, Commonwealth of Massachusetts.

Appendix A: maps of integrated intensities

As part of the data sets used for this work are so far only published in thesis works and thus not easily accessible, we present here maps of velocity integrated intensities of the five clouds L1457-S, S140, MCLD 126.6+24.5, NGC 1499 SW, and NGC 7538 (see Figs. 7-12). For a more detailed presentation we refer to the corresponding Ph.D. theses. The M17SW and Orion B-S data sets were presented in Stutzki & Güsten (1990) and Kramer et al. (1996).

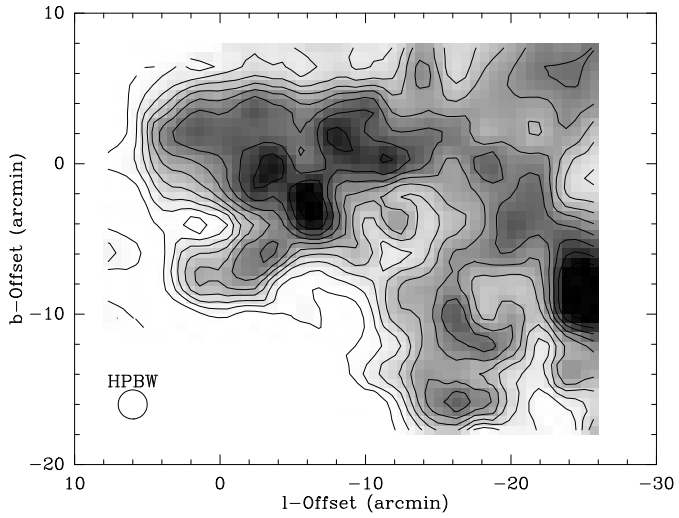

Fig. 9. Integrated ^{12}CO(2→1) emission of MCLD 126.6 + 24.5 observed with the KOSMA 3m telescope. The coordinate offsets are relative to l_{II} = 126.°6, b_{II} = 24.°535. The range of integration is −5.05 to −2.43 kms^{-1} and contours range from 0.2 (= 3σ) to 2.0 by 0.2 Kkms^{-1} (Corneliussen 1996).

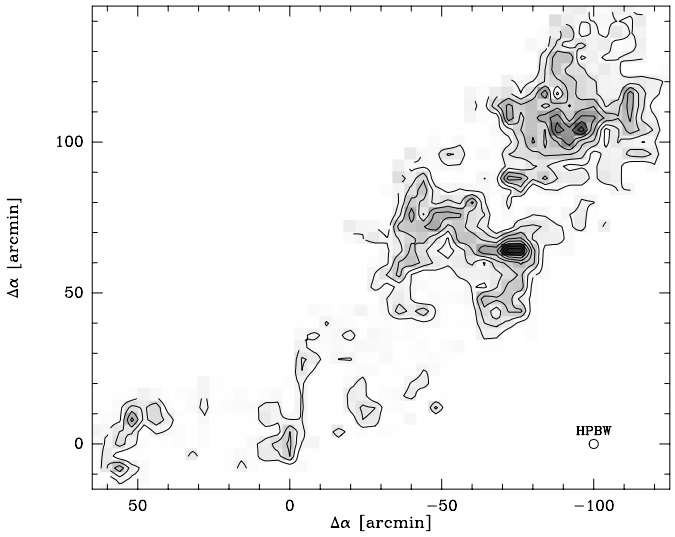

Fig. 10. Integrated ^{13}CO(1→0) emission of NGC 1499 SW observed with the Nagoya 4m telescope. The coordinate offsets are relative to $\alpha_0 = 3^h53^m28^s$, $\delta_0 = 37°02'$ (1950). The integration covers the range of emission from 1 (= 3σ) to 8 by 1 Kkms^{-1} (Herbertz 1992).

The contour levels of all maps presented here start at 3σ. The level spacing was selected to be 6σ for L1457 and 3σ for the 5 other maps. The σ values were calculated from the number of channels N per integration interval, the spectral resolution and the rms (Table 1), $\sigma = \sqrt{N}\Delta v_{\rm res} T_{\rm mb}^{\rm rms}$.

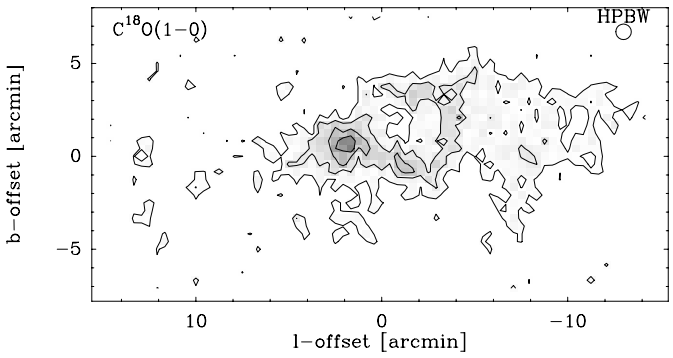

Fig. 11. Integrated C^{18}O(1→0) emission of NGC 7538 observed with the FCRAO 15m telescope. Coordinate offsets are relative to l_{II} = 111.5, b_{II} = 0.57 for both maps. Contour levels of temperatures integrated between −70 and −40 kms^{-1} range from 2.0 (∼ 3σ) to 8.0 by 2.0 Kkms^{-1} (Röhrig 1996).

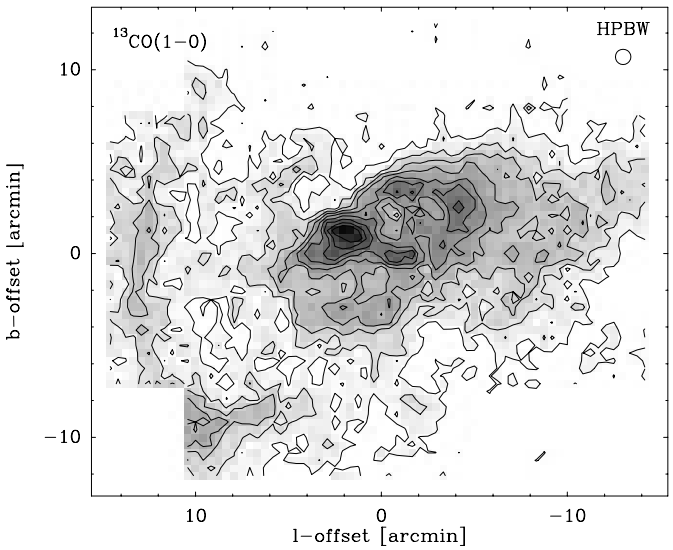

Fig. 12. Integrated ^{13}CO(1→0) emission of NGC 7538 taken with the FCRAO 15m telescope. The range of integration is −70 to −40 kms^{-1}. Contour levels range from 7.2 (∼ 3σ) to 72 by 7.2 Kkms^{-1} (Röhrig 1996).

References

Bevington P.R., Robinson D.K. 1992, Data reduction and error analysis for the physical sciences, McGraw-Hill, New York

Blitz L., 1993, Giant Molecular Clouds. In: Levy E.H., Lunine J.I. (eds.), Protostars and Planets III. The University of Arizona Press, Tuscon & London

Brand J., Wouterloot J.G.A., 1995, A&A, 303, 851

Carr J.S., 1987, ApJ, 323, 170

Casoli F., Combes F., Gerin M., 1984, A&A, 133, 99

Corneliussen U., 1996, Ph.D. thesis, University of Cologne

Das M., Jog C., 1996, ApJ, 462, 309

Dobashi K., Bernard J.P., Fukui Y., 1996, ApJ, 466, 282

Elmegreen B., Falgarone E., 1996, ApJ, 471, 816

Falgarone E., Phillips T.G., Walker C.K., 1991, ApJ, 378, 186

Green D.A., 1993, MNRAS, 262, 327

Heithausen A., Corneliussen U., 1995, The structure of the dense core in the high latitude cloud MCLD 126.6+24.5 In: Winnewisser G. (ed.) Proc. Zermatt, The Physics and Chemistry of Interstellar Molecular Clouds. Springer, Berlin

Herbertz R., 1992, Ph.D. thesis, University of Cologne
Herbertz R., Ungerechts H., Winnewisser G., 1991, A&A, 249, 483
Hobson M.P., 1992, MNRAS, 256, 457
Hobson M.P., Jenness T., Padman R., Scott P.F., 1994, MNRAS, 266, 972
Johnen C., 1992, Diplom thesis, University of Cologne
Kramer C., 1992, Ph.D. thesis, University of Cologne
Kramer C., Stutzki J., Winnewisser G., 1996, A&A, 307, 915
Lada E.A., 1992, ApJ, 393, L25
Lada E.A., Lada C.J., 1995, AJ, 109, 1682
Lada E.A., Bally J., Stark A.A., 1991a, ApJ, 368, 432
Lada E.A., DePoy D.L., Evans II N.J., Gatley I., 1991b, ApJ, 371, 171
Langer W.D., Wilson R.W., Anderson C.H., 1993, ApJ, 408, L45
Langer W.D., Velusamy T., Kuiper T.B.H., et al., 1995, ApJ, 453, 293
Lemme C., Walmsley C.M., Wilson T.L., Muders D., 1995, A&A, 302, 509
Loren R.B., 1989, ApJ, 338, 902
McCaughrean M.J., Stauffer J.R., 1994, AJ, 108, 1382
Moriarty-Schieven G.H., Anderesson B-G, Wannier P.G., 1997, ApJ, 475, 642
Nozawa S., Mizuno A., Teshima Y., et al., 1991, ApJS, 77, 647
Pound M.W., Blitz L., 1993, ApJ, 418, 328
Pound M.W., Blitz L., 1995, ApJ, 444, 270
Röhrig R., 1996, Ph.D. thesis, University of Cologne
Röhrig R., Stutzki J., Ungerechts H., Winnewisser G., 1995, Low-J-CO multiline studies of molecular clouds: NGC 7538 and others. In: Winnewisser G. (ed.) Proc. Zermatt, The Physics and Chemistry of Interstellar Molecular Clouds. Springer, Berlin
Salpeter E.E., 1955, ApJ, 121, 161
Sanders D.B., Scoville N.Z., Solomon P.M., 1985, ApJ, 289, 373
Scalo J.M., 1985, Fragmentation. In: Black D.C., Matthews M.S. (eds.), Protostars and Planets II. The University of Arizona Press, Tuscon
Silk J., 1995, ApJ, 438, L41
Solomon P.M., Rivolo A.R., 1989, ApJ, 339, 919
Stutzki J., Güsten R., 1990, ApJ, 356, 513 (SG90)
Stutzki J., Heithausen A., Bensch F., 1997, On the fractal structure of molecular clouds. In: Latter, W.B. et al. (eds.), CO: Twenty-five years of millimeter-wave spectroscopy, Proc. of the 170th IAU symposium. Kluwer Academic Publishers, Dordrecht/Boston/London
Tatematsu K., Umemoto T., Kameya O., et al., 1993, ApJ, 404, 643
Ungerechts H., Thaddeus P., 1987, ApJS, 63, 645
Wang Y., Jaffe D.T., Evans II N.J., et al., 1993, ApJ, 419, 707
Wiesemeyer H., Güsten R., Wink J.E., Yorke H.W., 1996, A&A, accepted
Williams J.P., De Geus E.J., Blitz L., 1994, ApJ, 428, 693
Williams J.P., Blitz L., Stark A.A., 1995, ApJ, 451, 252
Zimmermann T., 1993, Ph.D. thesis, University of Cologne
Zimmermann T., Stutzki J., 1993, Fractals, Vol.1, No.4, 930
Zimmermann T., Ungerechts H., 1990, A&A, 238, 337
Zinnecker H., 1989, Towards a theory in star formation. In: Beckman J. (ed.) Evolutionary phenomena in galaxies. Cambridge University Press, Cambridge
Zinnecker H., McCaughrean M.J., Wilking B.A., 1993, The initial stellar population. In: Levy E.H., Lunine J.I. (eds.), Protostars and Planets III. The University of Arizona Press, Tuscon & London

This article was processed by the author using Springer-Verlag LaTeX A&A style file *L-AA* version 3.